ARTICLES
https://doi.org/10.1038/s41563-018-0268-1
nature materials

Three-dimensional printing of piezoelectric materials with designed anisotropy and directional response

Huachen Cui[1], Ryan Hensleigh[2], Desheng Yao[1], Deepam Maurya[1], Prashant Kumar[1], Min Gyu Kang[1], Shashank Priya[1,3] and Xiaoyu (Rayne) Zheng[1,2]*

Piezoelectric coefficients are constrained by the intrinsic crystal structure of the constituent material. Here we describe design and manufacturing routes to previously inaccessible classes of piezoelectric materials that have arbitrary piezoelectric coefficient tensors. Our scheme is based on the manipulation of electric displacement maps from families of structural cell patterns. We implement our designs by additively manufacturing free-form, perovskite-based piezoelectric nanocomposites with complex three-dimensional architectures. The resulting voltage response of the activated piezoelectric metamaterials at a given mode can be selectively suppressed, reversed or enhanced with applied stress. Additionally, these electromechanical metamaterials achieve high specific piezoelectric constants and tailorable flexibility using only a fraction of their parent materials. This strategy may be applied to create the next generation of intelligent infrastructure, able to perform a variety of structural and functional tasks, including simultaneous impact absorption and monitoring, three-dimensional pressure mapping and directionality detection.

The direct piezoelectric constant correlates the electric displacement of a material with an applied stress[1–3]. Owing to their ability to convert mechanical to electrical energy and vice versa, piezoelectric materials have widespread applications in pressure sensing[4,5], ultrasonic sensing[6,7], actuation[8,9] and energy harvesting[10,11]. The piezoelectric charge constants of bulk piezoelectric ceramics, polymer-piezoelectric composites and their respective foams are dictated by their intrinsic crystallographic structures and compositions[12], resulting in common coupling modes of operation[13]. Additionally, their intrinsic microstructures are strongly coupled with other physical properties, including mass densities and mechanical properties[14]. Chemical modifications such as doping[15,16] have been introduced to change the piezoelectric constants in certain directions by altering the crystallographic structures, but their design space is restricted by the limited set of doping agents[17]. It also comes at the cost of other coupled physical properties such as mechanical flexibility and sensitivity[18,19]. Casting and templating techniques have been used to produce piezoelectric foams[20,21] that showcase the potential for reduced mass densities and improved hydrostatic figures of merit, but their piezoelectric coefficients, described by a square foam model[22], are largely limited by the intrinsic crystalline orientation and occupy only a narrow area within piezoelectric anisotropy space.

Here we report a set of concepts in which a wealth of direct piezoelectric responses can be generated through rationally designed piezoelectric architectural units and are realized via additive manufacturing of highly sensitive piezo-active lattice materials. Our strategy begins by designing families of three-dimensional (3D) structural node units assembled from parameterized projection patterns, which allows us to generate and manipulate a set of electric displacement maps with a given pressure, thereby achieving full control of piezoelectric constant tensor signatures. These unit cells are then tessellated in three dimensions, forming metamaterial blocks that occupy a vast piezoelectric anisotropy design space, enabling arbitrary selection of the coupled operational mode. Upon polarizing the as-fabricated piezoelectric material, we have demonstrated that piezoelectric behaviour in any direction can be selectively reversed, suppressed or enhanced, achieving distinct voltage response signatures with applied stress.

To implement this concept, we prepared functionalized lead zirconate titanate (PZT) nanoparticle colloids. These nanoparticles are then covalently bonded with entrapped photo-active monomers. These concentrated piezoelectric colloids are subsequently sculpted into arbitrary 3D form factors through high-resolution additive manufacturing. We found that building blocks with designed piezoelectric signatures could be assembled into intelligent infrastructures to achieve a variety of functions, including force magnitude and directionality sensing, impact absorption and self-monitoring, and location mapping, without any additional sensing component. These free-form PZT nanocomposite piezoelectric metamaterials not only achieve a high piezoelectric charge constant and voltage constant at low volume fractions but also simultaneously possess high flexibility, characteristics that have not been attainable in previous piezoelectric foams or polymers. This study paves the way for a class of rationally designed electromechanical coupling materials, thus moving structural metamaterials[23,24] towards smart infrastructures.

Design of 3D piezoelectric responses

We developed a strategy to realize the full design space of piezoelectric coefficients through the spatial arrangement of piezoelectric ligaments. Our scheme involves analysing configurations of projection patterns from a 3D node unit classified by connectivity. The evolutions of projection patterns give rise to diverse electric displacement maps (Fig. 1a–h), from which the piezoelectric

---

[1]Department of Mechanical Engineering, Virginia Tech, Blacksburg, VA, USA. [2]Macromolecules Innovation Institute, Virginia Tech, Blacksburg, VA, USA. [3]Materials Research Institute, Pennsylvania State University, University Park, PA, USA. *e-mail: raynexzheng@vt.edu

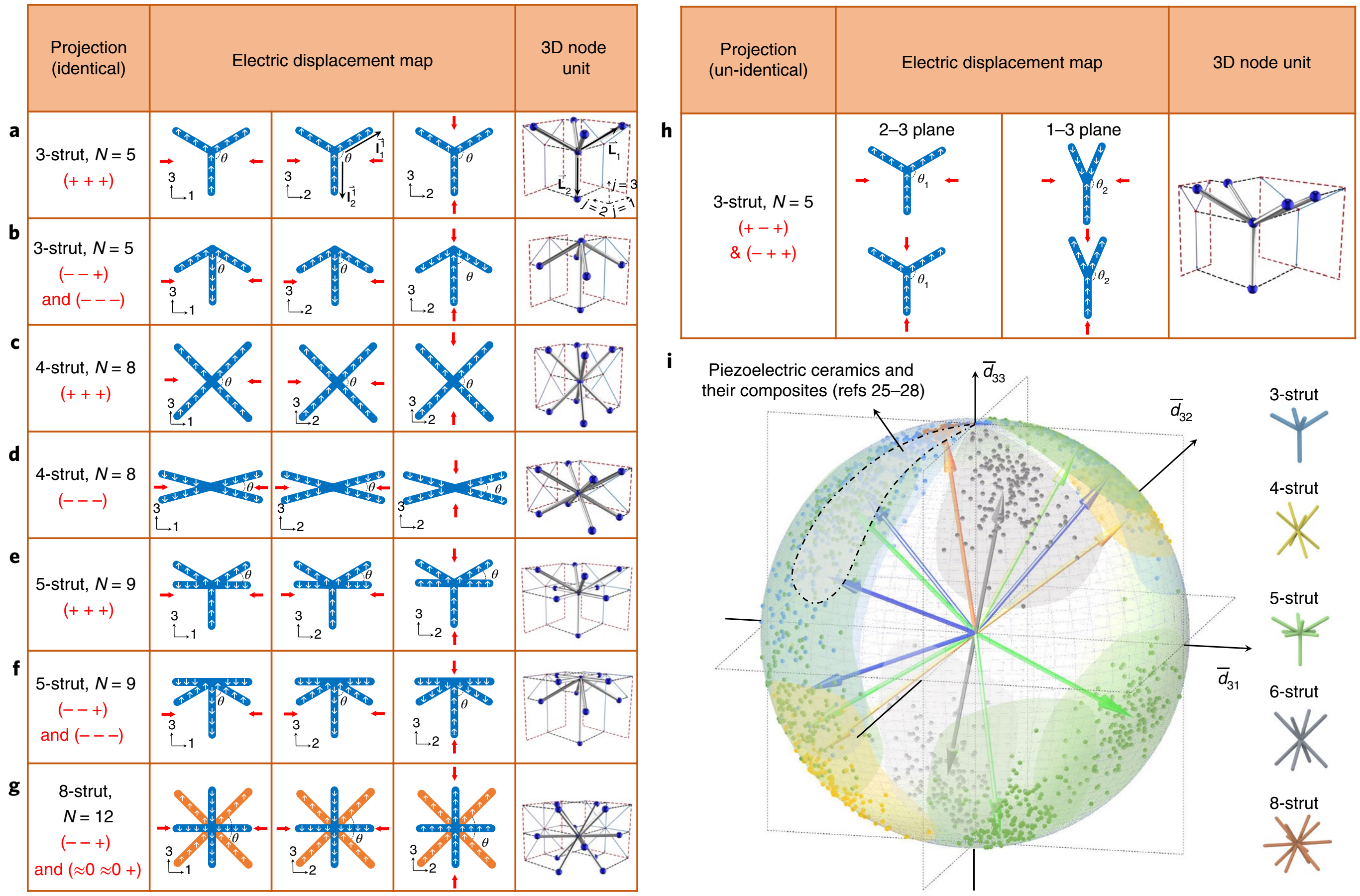

Fig. 1 | Design of piezoelectric metamaterials for tailorable piezoelectric charge constants. Designing 3D node units by configuring the projection patterns. **a**–**g**, Node unit designs from 3-, 4-, 5- and 8-strut identical projection patterns, respectively. A node unit with higher nodal connectivity can be constructed by superposition of projection patterns comprising a smaller number of projected struts. **h**, Node unit with dissimilar projection patterns showing decoupled $\bar{d}_{31}$, $\bar{d}_{32}$. The white arrows in the projection patterns pointing towards the positive or negative 3-direction indicate the positive or negative electric displacement contribution to poling direction 3. Red arrows in **a**–**h** indicate the compression loading along the 1-, 2- or 3-direction. **i**, A dimensionless piezoelectric anisotropy design space accommodating different 3D node unit designs with distinct d_{3M} distributions; each d_{3M} is normalized by the length of the vector {d_{31},d_{32},d_{33}} and thus $\bar{d}_{31}$, $\bar{d}_{32}$ and $\bar{d}_{33}$ form a right-handed 3D coordinate system. The dimensionless piezoelectric coefficients of their parent monolithic piezoelectric ceramics and their composites are labelled within the dashed region, {−−+} quadrant[25–28].

coefficient tensor space d_{3M} ($M=1$–3) can be designed, going beyond the limitations of the monolithic piezoelectric ceramics, polymers and their composite feedstock whose piezoelectric coefficients are located in the {−−+} quadrants[25–28] and {++−} quadrants[29,30]. Here the dimensionless piezoelectric tensor space, $\bar{\mathbf{d}}_{3M}$, is defined by normalizing d_{3M} by the length of the vector {d_{31}, d_{32}, d_{33}}. To capture the broadest possible design space, we start with the minimum number of intersecting microstruts at a node that can be tessellated into 3D periodic lattices. All intersecting struts are represented as vectors originating from the node, that is, $\mathbf{L}_i$ ($i=1$–N, where N is the node unit connectivity). In building our projection patterns, we define $\mathbf{l}_i^j$ as the 2D projection of $\mathbf{L}_i$ onto three orthogonal planes through the global 1–2–3 coordinate system of the 3D piezoelectric cube (Fig. 1a, $\mathbf{L}_i=\frac{1}{2}\sum_j^3\mathbf{l}_i^j$, where $j=1$, 2 or 3). As an example, we use piezoelectric ceramic and its composites, which have $\bar{\mathbf{d}}_{3M}$ distributed in the {−−+} quadrants[25–28], as the base material with which to construct the electric displacement maps. The white arrows pointing upwards or downwards against the 3-direction indicate the positive or negative electric displacement response of the strut along the 3-direction (that is, the poling direction).

Configuring the projection patterns in these planes results in diverse electric displacement maps, allowing access to different quadrants of the d_{3M} property space (Supplementary sections 1 and 2). A basic 3D node unit containing 3, 4 and 5 intersecting struts on the projection patterns is illustrated in Fig. 1a–f. We start with 3D node units with identical 3-strut projection patterns on the 1–3 and 2–3 planes, that is, $d_{31}=d_{32}$ (Fig. 1a,b). Configuring the projection pattern by rotating the relative orientations of two of the projected struts ($\theta=\angle\mathbf{l}_1^1\mathbf{l}_2^1$) redistributes the electric displacement contributions, as indicated by the white arrows reversing direction in the projection pattern (Fig. 1a,b). Rotating the projection patterns allows us to inversely reorient the intersecting spatial struts with correlations as calculated in Supplementary sections 1 and 2. This results in the $\bar{\mathbf{d}}_{3M}$ tensor shifting from the {+++} quadrant to highly anisotropic distribution near the positive $\bar{d}_{33}$ axis {0 0+} and then to the {−−+} quadrant with negative d_{31} and d_{32} as well as positive d_{33} (Fig. 1i). Further decrease of the relative orientation reverses all values of the d_{3M} to occupy the {−−−} quadrant (Supplementary Table 1). Similarly, for a 4-strut or 5-strut projection pattern with two-axis symmetry, decreasing the relative orientation ($\theta=\angle\mathbf{l}_1^1\mathbf{l}_2^1$ of projected struts) results in a change of d_{3M} distribution from the {+++} quadrant to the {−−−} quadrant (Fig. 1i) or the {−−+} quadrant owing to the competition of the opposite electric displacement contributions within the struts (Fig. 1c–f).

Our designs can be broadened by increasing the 3D node unit connectivity through superposition (Fig. 1g). Micro-architectures

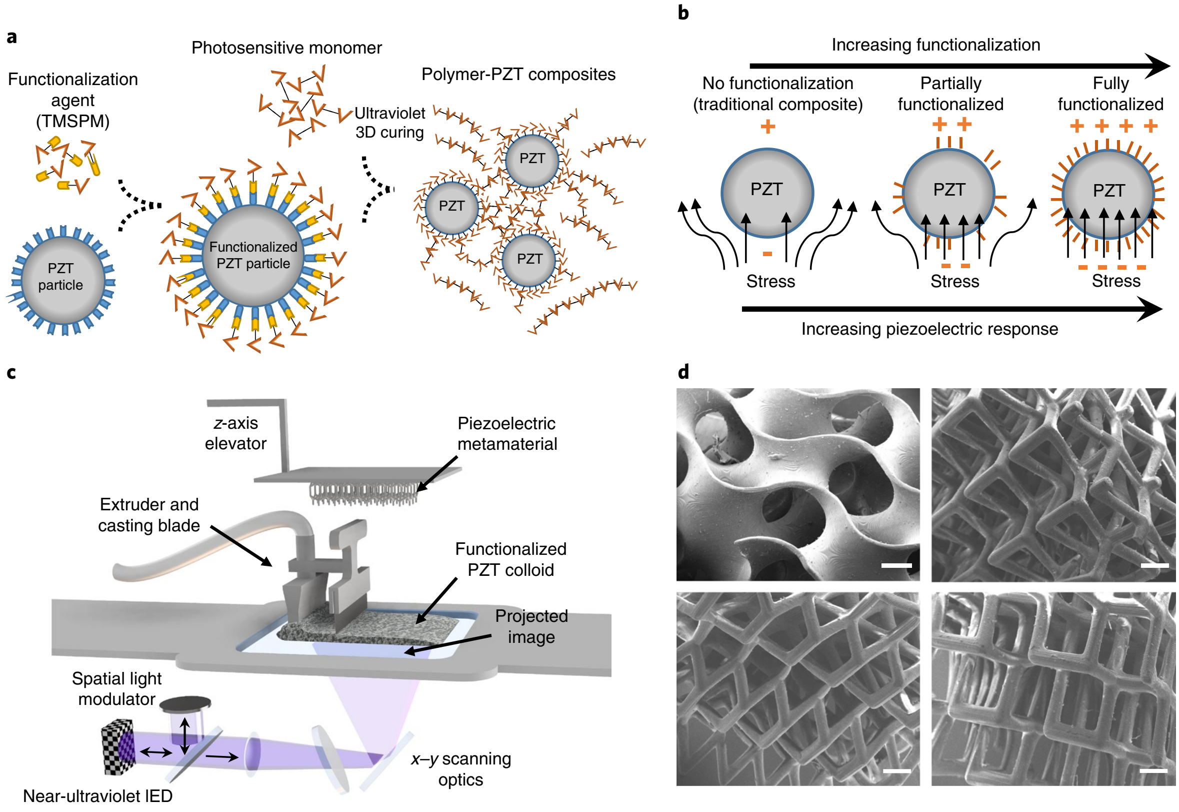

Fig. 2 | Surface functionalization of PZT with photosensitive monomers and 3D printing of piezoelectric metamaterials with complex micro-architectures. a, Schematic illustration of surface functionalization method and strong bonds between the nanoparticles and the polymer matrix after the ultraviolet curing process. **b**, Schematic illustration of the relationship between the surface functionalization level and the piezoelectric response. The piezoelectric response increases with the surface functionalization level as a result of increasing stress transfer. **c**, Schematic illustration of the high-resolution additive manufacturing system. **d**, Scanning electron microscope images of 3D-printed piezoelectric microlattices. Scale bars, 300 µm.

with high nodal connectivity are deformed mainly by compression or tension[31,32]. The d_{33} increases with additional nodal connectivity as compared to lower-connectivity cases in which strain energy from strut bending does not contribute to the electric displacement in the 3-direction.

Moreover, our designs are not restricted to identical projection patterns where d_{31} and d_{32} are coupled. 3D node unit designs with dissimilar projection patterns allow independent tuning of d_{31} and d_{32} ('out of 45° plane' distribution of d_{3M}, Fig. 1i, $d_{31} \neq d_{32}$). We configure the dissimilar electric displacement maps by independently varying the relative orientations θ_1 and θ_2 on the 1–3 and 2–3 planes (Fig. 1h, Supplementary Table 1). The compression along the 1-direction and 2-direction on the 3D node unit therefore generates different electric displacement maps and results in the decoupling of d_{31} and d_{32} (Fig. 1h).

The d_{nM} of designed units can be computed by collecting the electric displacement from all intersecting strut members $\mathbf{L}_i$ at equilibrium under applied stress. Such models relate the configuration of the projection patterns $\mathbf{l}_i^j$ with the piezoelectric coefficient of interest d_{nM} of the metamaterials (see derivations in Methods)

$$d_{nM} = \frac{\sum_{i=1}^{N}\int_{V_i}\mathbf{d}^i_{nm}\mathbf{T}^i_{mr}\boldsymbol{\sigma}^i_r dV_i}{\sum_{i=1}^{N}\int_{V_i}\boldsymbol{\delta}_{Mm}\mathbf{T}^i_{mr}\boldsymbol{\sigma}^i_r dV_i},$$

where $\mathbf{d}^i_{nm}$ is the piezoelectric coefficient matrix of the base material ($n = 1,2,3$, $m,M = 1$–6), $\mathbf{T}^i_{mr}$ represents the stress-transformation matrix from the local x–y–z coordinate system to the global 1–2–3 coordinate system, $\boldsymbol{\sigma}^i_r$ is the stress vector in the local coordinate system ($r = xx,yy,zz,xy,xz,yz$), V_i is the volume of the ith strut in the node unit and $\boldsymbol{\delta}_{Mm}$ is the Kronecker delta (Methods, Supplementary sections 1 and 2, Supplementary Figs. 1–4). Configuring the projection patterns generate various designs of architectures that occupy different quadrants of the $\bar{\mathbf{d}}_{3M}$ distribution space, as shown in Fig. 1i, where $M = 1$–3. These families of 3D node units constitute a broad 3D piezoelectric constant selection where d_{3M} occupy desired quadrants of the property space, in contrast to the piezoelectric coefficients obtained by piezoelectric square foam models[22] (Supplementary section 1, Supplementary Fig. 5). This rich design space creates an enormous palette of novel applications, as demonstrated in later sections.

Synthesis and printing of electromechanical metamaterials

Our fabrication method of 3D piezoelectric architectures starts by synthesizing surface-functionalized piezoelectric nanoparticles (Fig. 2a,b, see Supplementary section 3, Supplementary Table 2 for particle properties), dispersing them with ultraviolet-sensitive monomers into highly concentrated, uniform colloids (PZT volume loading up to 50%) that can be sculpted into 3D structures by near-ultraviolet light[33] (Fig. 2c). While surface functionalization of approximately 4 vol% piezoelectric nanoparticles has produced an appreciable piezoelectric coefficient as compared to non-functionalized dispersion[33], the trade-off between high piezoelectric responsiveness and processability has limited the realizations of arbitrary piezoelectric 3D micro-architectures with high piezoelectric coefficients. As shown in Fig. 2a, a functionalization agent, (trimethoxysilyl propyl methacrylate) is covalently grafted to the PZT particle

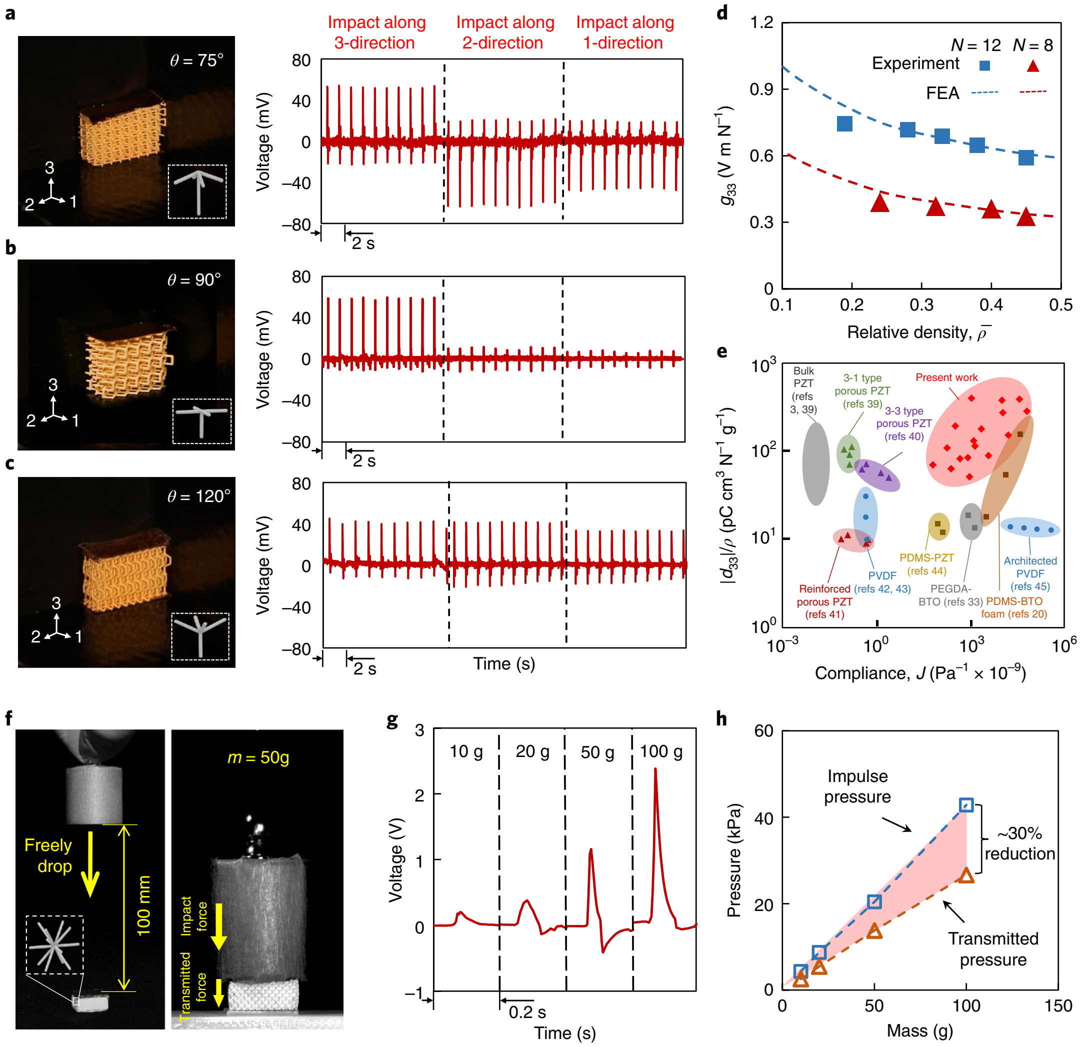

Fig. 3 | Measurement of 3D piezoelectric responses. a–c, Optical images of representative piezoelectric metamaterials comprised of $N=5$ node units and their corresponding real-time voltage outputs under impact coming from the 1-, 2- and 3-directions, respectively. **d**, Experimental and finite element analysis (FEA) results of the effective piezoelectric voltage constant g_{33}^{eff} versus the relative density of $N=8$ and $N=12$ lattice materials. **e**, Comparison of specific piezoelectric charge coefficients and elastic compliance between the piezoelectric metamaterials presented in this study and typical piezoelectric materials[3,20,33,39–45]. **f**, Drop-weight impact test on the as-fabricated piezoelectric lattice ($N=12$). **g**, The real-time voltage output of the lattice corresponding to various drop weights. The transient impact stress activates the electric displacement of the metamaterial in the 3-direction, shown as the trace of the voltage output against the impact time. **h**, Impulse pressure and transmitted pressure versus the mass of the drop weights. The significant gap (shaded area) between the detected impulse pressure and transmitted pressure reveals simultaneous impact energy absorption and self-monitoring capability of the 3D piezoelectric metamaterial.

surface via siloxide bonds leaving free methacrylate on the surface. The surface functionalization reaction is optimized to maximize surface coverage. These strong covalent bonds between the piezoelectric nanoparticles and the polymer matrix network improve the dispersion quality of the highly concentrated piezo-active colloidal resin (Supplementary section 4, Supplementary Figs. 6 and 7) by creating a sterically hindered surface. Increasing the functionalization level elevates the piezoelectric output of the nanocomposite to reach the upper bound at a given loading concentration (Fig. 2b, Supplementary section 5, Supplementary Fig. 8). Strict control of the thickness of the colloidal paste through the designed recoating system and reduction of oxygen inhibition enable the fabrication of complex 3D piezo-active architectures with fine features (Methods, Supplementary section 6) from a range of concentrated colloidal particles entrapped with ultraviolet-sensitive monomers (Fig. 2c–d, Supplementary Figs. 9–11). This versatile process is not limited to PZT. Surface functionalization can be implemented to enhance the response of a wide range of piezoelectrics (for example, barium titanate, BTO) or other functional materials such as multiferroics (for example, bismuth ferrite). The as-fabricated nanocomposite system does not require post-heat treatment, and achieves high structural fidelity and uniformity. Configuring the photo-sensitive monomer compositions enables independent tuning of the composite stiffness, allowing us to access rigid to flexible piezo-active materials to convert mechanical stress to voltage signals (Supplementary section 7, Supplementary Figs. 12–14, Supplementary Table 3, Supplementary Videos 1, 2), as well as energy harvesting (Supplementary section 7, Supplementary Fig. 15).

Measurement of 3D piezoelectric responses

To evaluate the piezoelectric responses of the designed piezoelectric metamaterials, we printed cubic lattices comprised of periodic unit

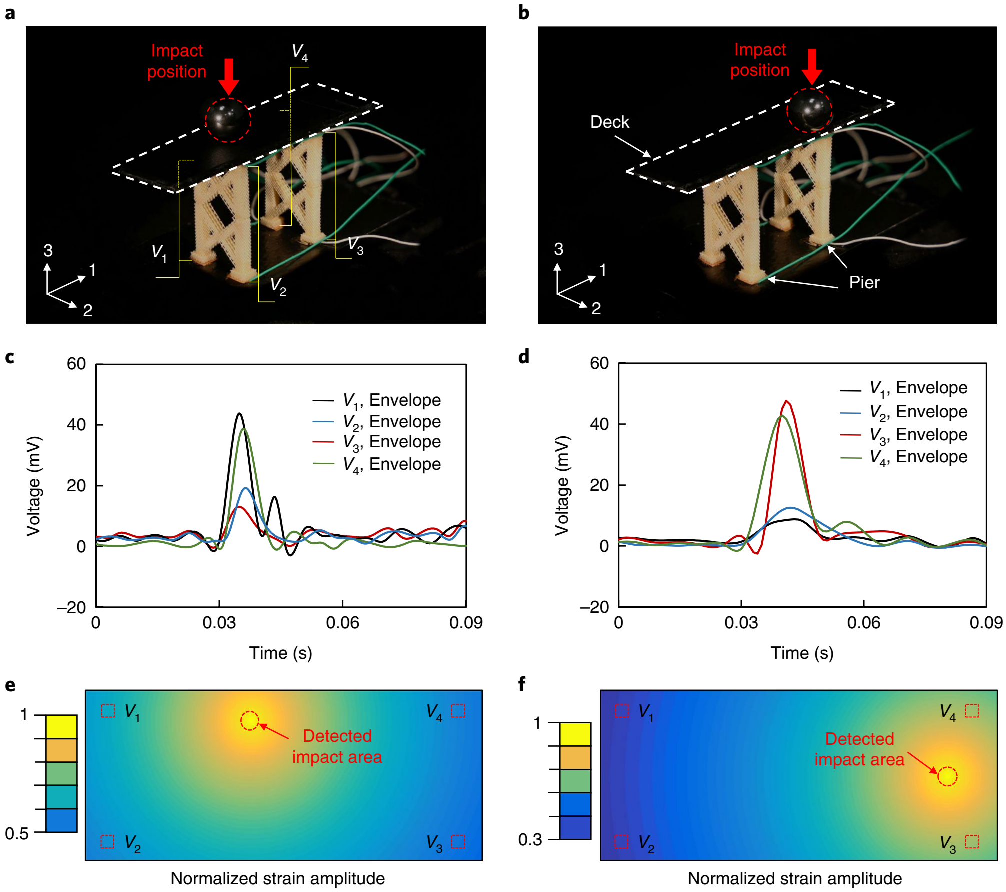

Fig. 4 | Assembly of architected metamaterial blocks as intelligent infrastructures. a,**b**, Camera image of a self-monitoring 3D-printed piezoelectric bridge infrastructure. All four piers are poled together along the 3-direction and the electrodes are attached to the top and bottom surface of the piers. V_1 to V_4 denote the voltage output between the corresponding electrodes. The locations of the dropping steel ball are indicated with dashed lines. **c**,**d**, Real-time voltage outputs from the self-monitoring piezoelectric piers. **e**,**f**, The normalized strain amplitude map (colour scale) converted from the voltage map indicates the different locations of the impact.

cells stacked along the three principal directions and poled them under uniform electric fields (see Methods, Supplementary section 8, Supplementary Figs. 16 and 17 for poling the samples). A shaker with an integrated force sensor exerts cyclical loadings on the samples (details in Supplementary section 9). We measured the generated voltages (in the 3-direction) induced by the applied stress with a resistor (40 MΩ) connected to a data acquisition system. We found excellent agreement of the measured $\{d_{31},d_{32},d_{33}\}$ signatures with the designed response to force from different directions. Here, $N=5$ designs (3-strut projection pattern, Fig. 1a,b) are used to demonstrate the different voltage output patterns due to the distinct distributions of d_{3M}. As identical cyclic loadings (about 0.5 N, sawtooth loading profile) are applied along three orthogonal directions, significant differences in the voltage output patterns are observed for three distinct designs (Fig. 3a–c, Supplementary Video 3; the voltage responses generated from square-loading and unloading profile are shown in Supplementary Fig. 18). The $N=5$ piezoelectric metamaterial of $\theta=75°$ (Fig. 3a) outputs a positive voltage when loaded in the 3-direction, while the sample generates a negative voltage when loaded in the 1- or 2-direction. In contrast, Fig. 3b shows that the voltage outputs of our $N=5$, $\theta=90°$ lattice in the 3-direction are positive while voltage output in the 1- or 2- direction is suppressed, exhibiting highly anisotropic response. By further increasing θ to 120°, the voltage outputs in all 1-, 2- and 3-directions are positive when loaded in any direction, as shown in Fig. 3c, owing to its all-positive d_{3M} distribution.

To assess the mechanical-electrical conversion efficiency, the effective piezoelectric voltage constant g_{33}, defined as the induced electrical field per unit applied stress, was quantified by measuring the d_{33} and permittivities of the as-fabricated metamaterials. The resistor used in the apparatus is replaced by a circuit to quantify the charge generated in response to applied stress (Supplementary Fig. 19, Supplementary section 9, Supplementary Table 4). The d_{33} and g_{33} are then quantified by the ratio of the applied load and the generated charge. The g_{33} results of the metamaterial comprised of highly connected structure ($N=12$ and $N=8$) are shown in Fig. 3d (see Supplementary section 10, Supplementary Fig. 20 for more details). Remarkably, g_{33} increases with decreasing relative density, indicating a potential application as a simultaneously light-weight and highly responsive sensor. The measured d_{33} over their mass density (that is, $|d_{33}|/\rho$) and compliance are plotted against all piezoelectric materials (Fig. 3e, Supplementary section 11). We found that these low-density and flexible piezoelectric metamaterials achieve over twice the specific piezoelectric constant of piezoelectric polymer (for example, polyvinylidene fluoride, PVDF) and a variety of flexible piezoelectric composites (Fig. 3e, Supplementary Fig. 21). Additionally, enhancement of the hydrostatic figures of merit can be obtained via unit cell designs with all identical signs of the $g_{3M}\{+++\}$ and $d_{3M}\{+++\}$ coefficients (Supplementary Fig. 20). This enhanced piezoelectric constant along with the highly connected 3D micro-architecture makes the 3D piezoelectric metamaterial an excellent candidate for simultaneous impact absorption and

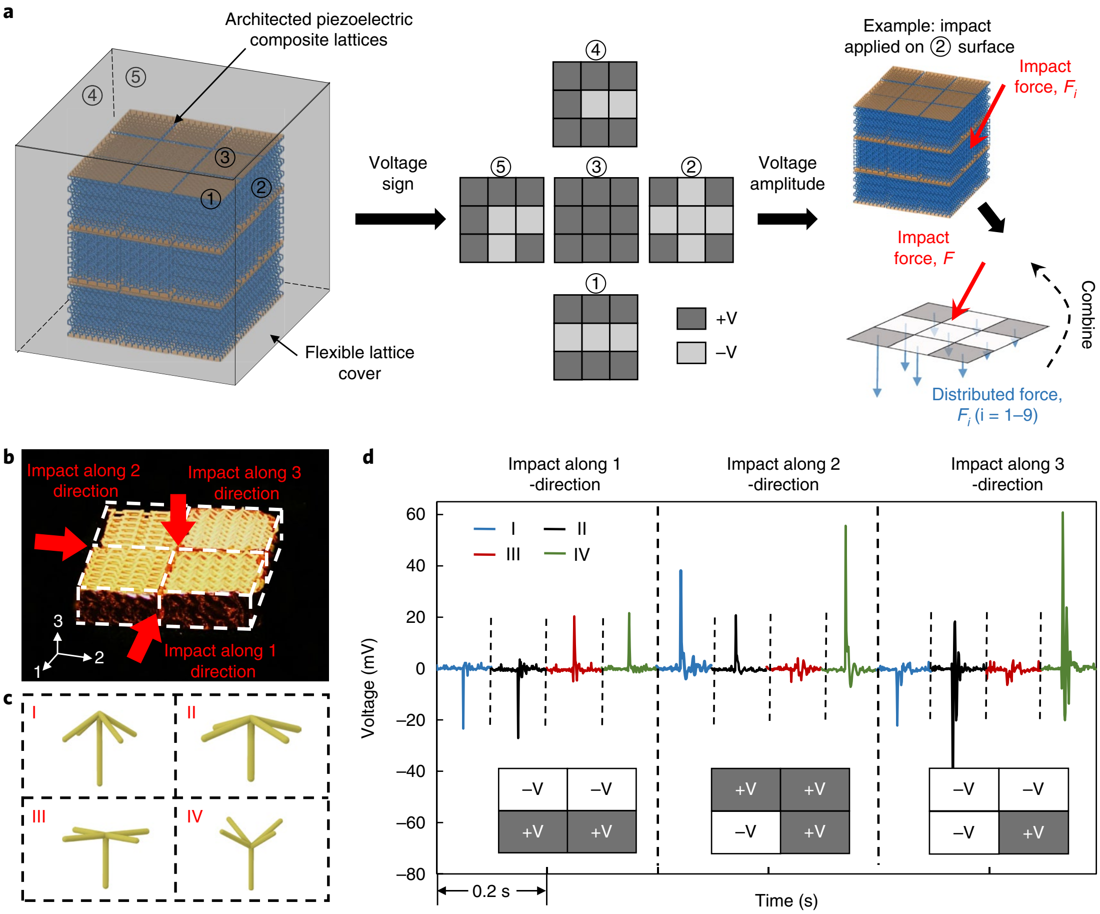

Fig. 5 | Force directionality sensing. a, Illustration of force directionality sensing application using piezoelectric metamaterials stacked from four types of designed building blocks to achieve arbitrary force directions. **b**, As-fabricated piezoelectric infrastructure comprised of stacked architectures with encoded piezoelectric constants. **c**, Voltage output patterns corresponding to different impact directions indicated by red arrows. The insets show the binary voltage patterns registered with different impact directions. The impact force in the 1-direction is registered with permutation voltage matrix [−,−,+,+], with [+,+,−,+] for the 2-direction and [−,−,−,+] for the 3-direction, respectively.

self-monitoring. A series of standard weights ranging from 10 g to 100 g were sequentially dropped onto the as-fabricated 3D piezoelectric lattice ($N=12$) attached on a rigid substrate (Fig. 3f) to impact the piezoelectric metamaterial (high-speed camera movie shown in Supplementary Video 4). The transient impact stress activates the electric displacement of the metamaterial in the 3-direction, shown as the trace of the voltage output against the impact time (Fig. 3g). The impulse pressure on the piezoelectric metamaterial calculated via the measured d_{33}, and the measured pressure transmitted to the rigid substrate against time are plotted in Fig. 3h. The significant gap (shaded area) between the impulse pressure and transmitted pressure reveals the impact energy absorption and protection capability of our piezoelectric 3D metamaterial as a potential smart infrastructure[34,35] (Supplementary sections 7 and 12, Supplementary Fig. 22).

Location and directionality sensing

The 3D digital metamaterial building blocks can be further stacked or printed as smart infrastructures capable of time-resolved pressure self-sensing and mapping without application of an external sensor. Here, piezoelectric metamaterials of $N=12$ are selected and 3D printed into a four-pier piezoelectric bridge with a non-piezoelectric bridge deck (Fig. 4a,b). The external closed circuits with a data acquisition system are connected to the top and bottom surfaces of the piers to monitor the voltage outputs. The 3D-printed piezoelectric metamaterial bridge can directly map the magnitude as well as the location of potentially damaging deformations throughout its structure. To demonstrate, steel balls with a mass of 8 g are sequentially dropped at random onto the deck. The resulting voltage is collected at each of the four electrodes with the amplitude depending on the electrode proximity. The envelopes of the voltage outputs (plotted in Fig. 4c,d) independently monitor the strain amplitude. The impact strain map of the deck can be plotted to determine the impact location (Fig. 4e,f, Supplementary section 13, Supplementary Fig. 23). These 3D piezoelectric infrastructures allow one to obtain time-resolved self-monitoring information (for example, displacements, forces, strain mapping) throughout a structure[36,37] without additional external sensors.

Taking advantage of the distinct directional d_{3M} design space, stacking multiple piezoelectric building blocks, each with a tailored directional response, allows us to program the voltage output patterns as binary codes (that is, positive or negative voltage). These stackable metamaterial blocks provide a method of determining directionality, which we leverage to sense pressure from arbitrary directions[38]. Figure 5a demonstrates the directionality sensing concept using sensing infrastructure assembled from an array of piezoelectric metamaterial cubes with pre-configured d_{3M} tensor signature $\{d_{31}, d_{32}, d_{33}\}$ distributed at different quadrants. Piezoelectric metamaterial cubes on the outer surface of the cube (surfaces 1 to 5, as labelled) are connected to voltage output channels, with intersecting faces of the cube sharing one voltage output channel (Supplementary Fig. 24). Pre-program stacked d_{3M} combinations with each face of the cube allows the output voltage binary map to be uniquely registered with a given pressure applied on that face. The direction and magnitude of any arbitrary force can then be super-positioned and determined from the collected voltage maps (Fig. 5a).

As a proof-of-concept demonstration of directionality sensing, we stacked a piezoelectric metamaterial infrastructure comprised of four cubic units with their unique, designed 3D piezoelectric signatures (Fig. 5b,c). The output voltage binary map uniquely registers the corresponding force direction. When impacted from the 1-, 2- and 3-directions (labelled I, II, III and IV in Fig. 5d), three distinct voltage outputs are detected, each correlated with the original respective impact direction (Fig. 5d, Supplementary Video 5). The impact force in the 1-direction is registered with permutation voltage matrix [−,−,+,+], with [+,+,−,+] for the 2-direction and [−,−,−,+] for the 3-direction, respectively (Fig. 5d). These digitalized, binary output voltage maps originated from the preconfigured piezoelectric constant signatures decode directionality of the impact as well as its magnitude.

Outlook

This work presents a method of designing electrical–mechanical coupling anisotropy and orientation effects, producing them via additive manufacturing (3D printing) of highly responsive piezoelectric materials. This creates the freedom to inversely design an arbitrary piezoelectric tensor, including symmetry conforming and breaking properties, transcending the common coupling modes observed in piezoelectric monolithic and foams. We see this work as a step towards rationally designed 3D transducer materials in which users can design, amplify or suppress any operational modes (d_{nM}) for target applications. Design and tessellation of the piezo-active units can lead to a variety of smart-material functionalities, including vector and tactile sensing, source detection, acoustic sensing and strain amplifications from a fraction of their parent materials. Whereas most 3D printing processes are capable of processing structural materials (polymer, metal or ceramics), multifunctional materials are particularly challenging owing to the inherent trade-off between processing compatibilities and functional properties. In this work, covalent bonding of concentrated piezoelectric nanocrystals with entrapped ultraviolet-sensitive monomers allows the attainment of high piezoelectric coefficients at a given volume loading. Our fabrication methods can be extended to lead-based or lead-free piezoelectric ceramics (PZT, BTO and so on) and other functional materials, allowing high-fidelity printing of complex 3D functional architectures. These 3D-printed multi-functional materials, with simultaneously tuned structural and transduction properties throughout their micro-architectures, eliminate requirements for sensor array deployment, suggesting applications from soft, conformable transducers to rigid, energy-absorbing smart structures.

Online content

Any methods, additional references, Nature Research reporting summaries, source data, statements of data availability and associated accession codes are available at https://doi.org/10.1038/s41563-018-0268-1.

Received: 17 May 2018; Accepted: 6 December 2018;
Published online: 21 January 2019

References

1. Ferren, R. A. Advances in polymeric piezoelectric transducers. *Nature* **350**, 26–27 (1991).
2. Anderson, J. C. & Eriksson, C. Piezoelectric properties of dry and wet bone. *Nature* **227**, 491–492 (1970).
3. Priya, S. & Nahm, S. *Lead-free Piezoelectrics* (Springer, New York, 2011).
4. Li, F. et al. Ultrahigh piezoelectricity in ferroelectric ceramics by design. *Nat. Mater.* **17**, 349–354 (2018).
5. Guerin, S. et al. Control of piezoelectricity in amino acids by supramolecular packing. *Nat. Mater.* **17**, 180–186 (2018).
6. Egusa, S. et al. Multimaterial piezoelectric fibres. *Nat. Mater.* **9**, 643–648 (2010).
7. Lu, X., Qu, H. & Skorobogatiy, M. Piezoelectric micro- and nanostructured fibers fabricated from thermoplastic nanocomposites using a fiber drawing technique: comparative study and potential applications. *ACS Nano* **11**, 2103–2114 (2017).
8. Masmanidis, S. C. et al. Multifunctional nanomechanical systems via tunably coupled piezoelectric actuation. *Science* **317**, 780–783 (2007).
9. Wang, X. et al. Subatomic deformation driven by vertical piezoelectricity from CdS ultrathin films. *Sci. Adv.* **2**, e1600209 (2016).
10. Ganeshkumar, R., Cheah, C. W., Xu, R., Kim, S.-G. & Zhao, R. A high output voltage flexible piezoelectric nanogenerator using porous lead-free $KNbO_3$ nanofibers. *Appl. Phys. Lett.* **111**, 013905 (2017).
11. Gafforelli, G., Corigliano, A., Xu, R. & Kim, S.-G. Experimental verification of a bridge-shaped, nonlinear vibration energy harvester. *Appl. Phys. Lett.* **105**, 203901 (2014).
12. Dagdeviren, C. et al. Conformal piezoelectric systems for clinical and experimental characterization of soft tissue biomechanics. *Nat. Mater.* **14**, 728–736 (2015).
13. Grupp, D. E. & Goldman, A. M. Giant piezoelectric effect in strontium titanate at cryogenic temperatures. *Science* **276**, 392–394 (1997).
14. Espinosa, H. D., Bernal, R. A. & Minary-Jolandan, M. A review of mechanical and electromechanical properties of piezoelectric nanowires. *Adv. Mater.* **24**, 4656–4675 (2012).
15. Laurenti, M. et al. Nanobranched ZnO Structure: p-Type doping induces piezoelectric voltage generation and ferroelectric-photovoltaic effect. *Adv Mater* **27**, 4218–4223 (2015).
16. Shin, S. H. et al. Lithium-doped zinc oxide nanowires-polymer composite for high performance flexible piezoelectric nanogenerator. *ACS Nano* **8**, 10844–10850 (2014).
17. Harris, D. T., Burch, M. J., Mily, E. J., Dickey, E. C. & Maria, J. P. Microstructure and dielectric properties with CuO additions to liquid phase sintered $BaTiO_3$ thin films. *J. Mater. Res.* **31**, 1018–1026 (2016).
18. Nag, S. K. & Agrawal, D. C. Piezoelectric and mechanical-properties of ceria-doped lead zirconate titanate ceramics. *J. Mater. Sci.* **27**, 4125–4130 (1992).
19. Manna, S., Brennecka, G. L., Stevanović, V. & Ciobanu, C. V. Tuning the piezoelectric and mechanical properties of the AlN system via alloying with YN and BN. *J. Appl. Phys.* **122**, 105101 (2017).
20. McCall, W. R., Kim, K., Heath, C., La Pierre, G. & Sirbuly, D. J. Piezoelectric nanoparticle-polymer composite foams. *ACS Appl. Mater. Inter.* **6**, 19504–19509 (2014).
21. Smay, J. E., Tuttle, B. & III, J. C. *Piezoelectric and Acoustic Materials for Transducer Applications* 305–318 (Springer, Boston, 2008).
22. Challagulla, K. S. & Venkatesh, T. A. Electromechanical response of piezoelectric foams. *Acta Mater.* **60**, 2111–2127 (2012).
23. Zheng, X. et al. Ultralight, ultrastiff mechanical metamaterials. *Science* **344**, 1373–1377 (2014).
24. Bauer, J. et al. Nanolattices: An emerging class of mechanical metamaterials. *Adv. Mater.* **29**, 1701850 (2017).
25. Hashimoto, K. Y. & Yamaguchi, M. Elastic, piezoelectric and dielectric properties of composite materials. *IEEE 1986 Ultras. Symp.* **2**, 697–702 (1986).
26. Glushanin, S., Topolov, V. Y. & Krivoruchko, A. V. Features of piezoelectric properties of 0–3 $PbTiO_3$-type ceramic/polymer composites. *Mater. Chem. Phys.* **97**, 357–364 (2006).
27. Huang, J. H. & Kuo, W. S. Micromechanics determination of the effective properties of piezoelectric composites containing spatially oriented short fibers. *Acta Mater.* **44**, 4889–4898 (1996).
28. Bowen, C. R. & Topolov, V. Y. *Electromechanical Properties In Composites Based On Ferroelectrics* 1–202 (Springer, London, 2009).
29. Nix, E. L. & Ward, I. M. The measurement of the shear piezoelectric coefficients of polyvinylidene fluoride. *Ferroelectrics* **67**, 137–141 (1986).
30. Wang, H., Zhang, Q. M., Cross, L. E. & Sykes, A. O. Piezoelectric, dielectric, and elastic properties of poly(vinylidene fluoride/trifluoroethylene). *J. Appl. Phys.* **74**, 3394–3398 (1993).
31. Deshpande, V. S., Ashby, M. F. & Fleck, N. A. Foam topology bending versus stretching dominated architectures. *Acta Mater.* **49**, 1035–1040 (2001).
32. Cui, H. C., Hensleigh, R., Chen, H. S. & Zheng, X. Y. Additive manufacturing and size-dependent mechanical properties of three-dimensional microarchitected, high-temperature ceramic metamaterials. *J. Mater. Res.* **33**, 360–371 (2018).
33. Kim, K. et al. 3D optical printing of piezoelectric nanoparticle–polymer composite materials. *ACS Nano* **8**, 9799–9806 (2014).
34. Singhal, N., Sharma, M. & Mangal, S. K. Optimal placement of piezoelectric patches over a smart structure. *Integrated Ferroelectrics* **183**, 60–90 (2017).
35. Annamdas, V. G. M. & Soh, C. K. Influence of loading on the near field based passive metamaterial in structural health monitoring. *Strut. Health Monit.* **1**, 633–640 (2015).

36. He, X. M. et al. Synthetic homeostatic materials with chemo-mechano-chemical self-regulation. *Nature* **487**, 214–218 (2012).
37. Eliades, S. J. & Wang, X. Q. Neural substrates of vocalization feedback monitoring in primate auditory cortex. *Nature* **453**, 1102–1106 (2008).
38. Wu, W. Z., Wen, X. N. & Wang, Z. L. Taxel-addressable matrix of vertical-nanowire piezotronic transistors for active and adaptive tactile imaging. *Science* **340**, 952–957 (2013).
39. Liu, W. et al. Piezoelectric and mechanical properties of CaO reinforced porous PZT ceramics with one-dimensional pore channels. *Ceramics Int.* **43**, 2063–2068 (2017).
40. Bowen, C. R., Perry, A., Lewis, A. C. F. & Kara, H. Processing and properties of porous piezoelectric materials with high hydrostatic figures of merit. *J. Eur. Ceram. Soc.* **24**, 541–545 (2004).
41. Wang, J. X. et al. Microstructure, electrical and mechanical properties of MgO nanoparticles—reinforced porous PZT 95/5 ferroelectric ceramics. *Ceramics Int.* **39**, 3915–3919 (2013).
42. Pu, J. A., Yan, X. J., Jiang, Y. D., Chang, C. E. & Lin, L. W. Piezoelectric actuation of direct-write electrospun fibers. *Sensors Actuators A* **164**, 131–136 (2010).
43. He, X. J. & Yao, K. Crystallization mechanism and piezoelectric properties of solution-derived ferroelectric poly(vinylidene fluoride) thin films. *Appl. Phys. Lett.* **89**, 112909 (2006).
44. Babu, I. & de With, G. Highly flexible piezoelectric 0–3 PZT-PDMS composites with high filler content. *Composites Sci. Technol.* **91**, 91–97 (2014).
45. Fang, L. C., Li, J., Zhu, Z. Y., Orrego, S. & Kang, S. H. Piezoelectric polymer thin films with architected cuts. *J. Mater. Res.* **33**, 330–342 (2018).

Acknowledgements

We acknowledge funding from the ICTAS Junior Faculty Award, NSF CMMI 1727492, the Air Force Office of Scientific Research (FA9550-18-1-0299) and the Office of Naval Research (N00014-18-1-2553) for supporting this work. D.M. and S.P. acknowledge the financial support from NSF through award IIP-1832179. P.M. and M.G.K. are thankful for the support from Air Force Office of Scientific Research through grant FA9550-18-1-0233. We thank E. Ventrella, R. Mondschein and Dr. T. Long for help with collecting PZT particle diameter data, A. Wei, K. Jung, H. Chen, and Z. Xu for assitance with analysis and fabrication.

Author contributions

X.Z. conceived and designed the research. R.H. synthesized the functionalized piezoelectric materials and functionalization measurement. H.C. fabricated samples, performed testing and data analysis. D.Y. and H.C. designed the models and performed the analytical and numerical calculations. H.C., R.H. and X.Z. developed the materials and fabrication methods. D.Y., H.C. and X.Z. developed the method for manipulating anisotropy. D.M., P.K., M.G.K. and S.P. developed the poling method and contributed to the testing of the piezoelectric properties of the 3D metamaterials. H.C., R.H., D.Y. and X.Z. wrote the manuscript with input from all authors. All authors participated in drafting the manuscript, discussion and interpretation of the data.

Competing interests

The design and material fabrication methods have been submitted for pending US patents.

Additional information

Supplementary information is available for this paper at https://doi.org/10.1038/s41563-018-0268-1.

Reprints and permissions information is available at www.nature.com/reprints.

Correspondence and requests for materials should be addressed to X.Z.

Methods

Designing d_{3M} based on unit cell patterns. We developed an analytical model to establish the relationship between the piezoelectric charge constant tensor and the projection pattern parameters. The effective piezoelectric charge constant d_{nKL} is defined to correlate the induced effective electric displacement D_n of a 3D unit cell with applied stress σ_{KL} as follows:

$$D_n = d_{nKL}\sigma_{KL} \tag{1}$$

D_n, d_{nKL} and σ_{KL} represent the effective electric displacement field, the effective piezoelectric charge constant tensor, and externally applied stress field defined in the global 1–2–3 system, respectively (Fig. 1a, $n,K,L = 1–3$). We compute the d_{nKL} of a node unit under applied stress by collecting and volume-averaging the electric displacement contributions $D_n^{(i)}$ and stress in equilibrium with σ_{KL} from all strut members $\mathbf{L}_i$:

$$\begin{cases} D_n = \dfrac{1}{V}\displaystyle\sum_{i=1}^{N}\int_{V_i} D_n^{(i)}\mathrm{d}V_i \\ \sigma_{KL} = \dfrac{1}{V}\displaystyle\sum_{i=1}^{N}\int_{V_i} \boldsymbol{\delta}_{Kk}\boldsymbol{\delta}_{Ll}\boldsymbol{\sigma}_{kl}^{(i)}\mathrm{d}V_i \end{cases} \tag{2}$$

where V_i is the volume of the ith strut; V is the effective volume of the node unit cell; $\boldsymbol{\sigma}_{kl}^{(i)}$ is the stress state of the ith strut in the global 1–23 system, respectively, and $k,l = 1–3$; $\boldsymbol{\delta}_{Kk}$ and $\boldsymbol{\delta}_{Ll}$ represent the Kronecker delta to identify the stress components that are in equilibrium with the externally applied load. We introduce a local beam coordinate system $x–y–z$ for struts (Supplementary Fig. 4), and relate the stress in the global 1–2–3 system ($\boldsymbol{\sigma}_{kl}^{(i)}$) and local $x–y–z$ system ($\boldsymbol{\sigma}_{pq}^{(i)}$) by a linear transformation operator containing strut orientation information:

$$\boldsymbol{\sigma}_{kl}^{(i)} = \mathbf{N}_{kp}^{(i)}\boldsymbol{\sigma}_{pq}^{(i)}\left(\mathbf{N}_{lq}^{(i)}\right)^T \tag{3}$$

where $p,q = x, y, z$ and $N^{(i)}$ represents the coordinate system transformation matrix containing components with respect to the projection pattern angle (θ_j, $j = 1–3$)[46] and has the form:

$$\mathbf{N}^{(i)} = \begin{bmatrix} \cos\theta_2 & 0 & \sin\theta_2 \\ 0 & 1 & 0 \\ \sin\theta_2 & 0 & -\cos\theta_2 \end{bmatrix}\begin{bmatrix} 1 & 0 & 0 \\ 0 & \cos\theta_1 & \sin\theta_1 \\ 0 & \sin\theta_1 & -\cos\theta_1 \end{bmatrix}\begin{bmatrix} \cos\theta_3 & \sin\theta_3 & 0 \\ \sin\theta_3 & -\cos\theta_3 & 0 \\ 0 & 0 & 1 \end{bmatrix} \tag{4}$$

Substituting equation (3) into equations (1) and (2) yields the expression of the effective charge constants d_{nKL}:

$$\begin{aligned} d_{nKL} &= \frac{D_n}{\sigma_{KL}} \\ &= \frac{\sum_{i=1}^{N} A_i\ |L_i|\ \mathbf{d}_{nkl}\mathbf{N}_{kp}^{(i)}\boldsymbol{\sigma}_{pq}^{(i)}(\mathbf{N}_{lq}^{(i)})^T}{\sum_{i=1}^{N} A_i\ |L_i|\ \boldsymbol{\delta}_{Kk}\boldsymbol{\delta}_{Ll}\mathbf{N}_{kp}^{(i)}\boldsymbol{\sigma}_{pq}^{(i)}(\mathbf{N}_{lq}^{(i)})^T} \\ &= \frac{\sum_{i=1}^{N} \mathbf{d}_{nkl}\mathbf{N}_{kp}^{(i)}\boldsymbol{\sigma}_{pq}^{(i)}(\mathbf{N}_{lq}^{(i)})^T}{\sum_{i=1}^{N} \boldsymbol{\delta}_{Kk}\boldsymbol{\delta}_{Ll}\mathbf{N}_{kp}^{(i)}\boldsymbol{\sigma}_{pq}^{(i)}(\mathbf{N}_{lq}^{(i)})^T} \end{aligned} \tag{5}$$

where A_i and $|L_i|$ are the area of the cross-section and length of the ith strut, respectively. These two variables are assumed to be the same for all struts in the node unit.

This allows the design of d_{nKL}—or equivalently in Voigt notation, d_{nM}—according to the projection pattern configurations (by convention, $KL \rightarrow M$: $11\rightarrow1$; $22\rightarrow2$; $33\rightarrow3$; $12\rightarrow4$; $13\rightarrow5$; $23\rightarrow6$). We demonstrate the application of the method by designing d_{nM} according to the relative orientation θ between the projected struts (see examples in Supplementary sections 1 and 2, and Supplementary Figs. 1–4). Here, to convert the tensor notation ($KL \rightarrow M$), the coordinate system transformation matrix $\mathbf{N}^{(i)}$ (3×3 dimensions) is expanded and rearranged to form the stress transformation matrix $\mathbf{T}^{(i)}$ (6×6 dimensions).

Surface functionalization of the piezoelectric particles. All chemicals were purchased from Sigma-Aldrich and used as received. For functionalization, 0.6 g of PZT was ultrasonically dispersed (VWR Scientific Model 75 T Aquasonic, at about 90 W and about 40 kHz) in 50 g of deionized water with 1.049 g glacial acetic acid for 2 h. To this 1.049 g of 3-(trimethoxysilyl)propyl methacrylate (TMSPM) was added. The mixture was then refluxed while stirring. Particles were cleaned by centrifugation, followed by discarding the supernatant, and then dispersed in ethanol for at least two cycles. Particles were dried overnight under vacuum or gentle heat. The resulting 3D-printable functionalized PZT nanocomposites achieved a controlled volume loading from 2.5 vol% to 50 vol% (equivalent to 16 wt% to 88 wt%).

High-resolution projection stereolithography. The functionalized particles were sonicated in acetone and mixed with photosensitive resin for 3D printing; the acetone was then evaporated by gentle heat and stirring. High-resolution, large-area stereolithography systems were used for the piezoelectric architected material fabrication. Our 3D printing configurations for processing these colloidal piezoelectric feedstocks with a range of loading concentrations are described in Supplementary section 6 (Supplementary Figs. 9–11). The 3D models were built and sliced into 2D images using design method described in ref. [47] and Netfabb[48]. These 2D images are used to pattern light from a near-ultravioletlight-emitting diode (LED) using a programmable dynamic photomask. A reductive lens is used to isotropically reduce the near-ultraviolet light pattern to the desired length scale. A larger area build is generated by scanning and reflecting the light patterns within the horizontal $x–y$ plane while maintaining the resolution (Fig. 2c). Aligned with the optics is a substrate, which can be coated with the functionalized ultraviolet-sensitive colloidal paste to a controlled thickness. When illuminated, the colloid replicates the 2D image as a solid layer bound to the substrate or any previous layers. Recoating of the now-solidified layers and the substrate with the colloidal solution, followed by additional exposures from subsequent 2D image slices and synchronized movement of the precision stage, builds the 3D part with complex architectures. The as-fabricated piezoelectric lattices were measured to have strut thickness variation within 3% via X-ray microtomography using the method described in ref. [49].

Poling of the piezoelectric metamaterials. The corona poling method was used to pole the as-fabricated samples (Supplementary Fig. 16). The samples were placed on a planar electrode connected to a high-voltage power supply (Glassman High Voltage Inc., Series EK) and poled under 32 kV at room temperature for 1 h. The experimental setup was also equipped with a digital multimeter (Agilent 34410 A) for measuring the current through the sample under voltage. To avoid screening of the bottom electrode, we kept samples inside highly insulating liquids (details in Supplementary section 8, Supplementary Figs. 16 and 17).

Characterization of the piezoelectric metamaterials. To evaluate the effective piezoelectric charge constants, a piezoelectric testing fixture was set up to record the voltage output of the samples with loads being applied. The electric charges generated from the samples were calculated by multiplying the voltage output by the capacitance of the circuit (Supplementary Fig. 19b). The instrument was fully calibrated using two commercial PZT cylindrical samples with piezoelectric coefficients of 540 pC N^{-1} and 175 pC N^{-1} respectively (Supplementary Fig. 19c). The effect of triboelectrification was eliminated by comparing the measurements before and after polarizations (Supplementary Fig. 19d). To measure the signatures of the voltage output directly, a resistor with 40 MΩ resistance was connected to the sample and the voltage was directly measured from both ends of the resistor.

Finite element analysis. ABAQUS 6.14[50] was used to conduct the finite element analysis. The base material properties used are summarized in Supplementary section 14 and Supplementary Table 5. A ten-node quadratic piezoelectric tetrahedron (C3D10E) element was used to mesh the unit cells. Four degrees of freedom are allowed at each node: three translational degrees of freedom and one electrical potential degree of freedom. Periodic boundary conditions were applied to the node unit to capture the complete electromechanical response of the metamaterials[51]. Stresses are applied on the surfaces perpendicular to the 1-, 2- or 3-directions individually to calculate d_{3M}. Low strain and low linear deformation are also ensured.

Data availability

All data generated during this study are included within the paper and its Supplementary Information files and/or are available from the corresponding author upon request.

References

46. Wan, Hu,J. & Park, T. Continuum models for the plastic deformation of octet-truss lattice materials under multiaxial loading. *J. Eng. Mater. Technol.* **135**, 021004 (2013).
47. Zheng, X. et al. Multiscale metallic metamaterials. *Nat. Mater.* **15**, 1100–1106 (2016).
48. Netfabb, *Netfabb Ultimate 2019* (Autodesk, 2019).
49. Liu, L., Kamm, P., Garcia-Moreno, F., Banhart, J. & Pasini, D. Elastic and failure response of imperfect three-dimensional metallic lattices: the role of geometric defects induced by Selective Laser Melting. *J. Mech. Phys. Solids.* **107**, 160–184 (2017).
50. Abaqus, *Abaqus 6.14 Documentation* (Dassault Systèmes, 2014).
51. Kar-Gupta, R. & Venkatesh, T. A. Electromechanical response of piezoelectric composites: effects of geometric connectivity and grain size. *Acta Mater.* **56**, 3810–3823 (2008).